

1 **A decomposition of the atmospheric and surface contributions to the outgoing**
2 **longwave radiation**

3
4
5 Han Huang, Yi Huang

6 Department of Atmospheric and Oceanic Sciences, McGill University, Montreal, Canada
7
8
9
10
11

12 Corresponding Author: Han Huang, han.huang2@mcgill.ca (ORCID: 0000-0002-9143-6453)
13
14
15
16

Abstract

The outgoing longwave radiation (OLR), which consists of the thermal radiation from both the atmosphere and surface, is of critical importance to the Earth radiation energy budget. To understand the global OLR distribution, it is important to quantify the varying atmospheric and surface contributions. In this work, we present such a quantification using radiative transfer computations based on global reanalysis atmospheric data. By dissecting the OLR simulated following the radiative transfer equation, we quantitatively measure the layer-wise atmospheric contributions to OLR and compare it to the surface contribution in different spectral bands. One focus of this study is on the OLR in the far-infrared, for which new satellites are expected to provide unprecedented measurements. We find that around 45% of the global mean OLR is radiated in the far-infrared and in polar regions the far-infrared contribution can increase to 60%. Our vertical decomposition of OLR discloses that the enhanced far-infrared contribution in the polar regions mainly results from a stronger surface (as opposed to atmosphere) contribution. Our analysis also reveals that the tropopause layer makes a minimum contribution to the OLR, which may be a unique spectroscopic feature of the Earth atmosphere. Clouds are found to reduce the atmospheric contribution in the far-infrared while enhancing it in the mid-infrared.

(Plain Language Abstract)

OLR plays a fundamental role in Earth's energy budget. We quantify the layer-wise atmospheric contribution to OLR, with a focus on the radiation energy in the far-infrared. Combining the spectral, vertical and geographic perspectives, our analysis identifies the critical atmospheric layers that account for the OLR in different spectral ranges. Our results affirm the importance of far-infrared spectrum for the Earth radiation balance and reveal that the geographic variation of the OLR in far-infrared is mainly driven by a varying surface contribution.

Key Points

1. The higher FIR fraction of OLR in polar region is due to stronger surface contribution.
2. The atmospheric layer around the tropopause makes a minimum contribution to OLR.
3. Cloud radiative effect reduces the atmospheric contribution in FIR and increases it in MIR.

1. Introduction

The outgoing longwave radiation (OLR) at the top of the atmosphere (TOA) is an important component of the Earth's radiation energy budget. The balance between OLR and the net incoming solar radiation determines the energy gain or loss, and thus the thermal state, of the whole climate system. OLR consists of the atmospheric emission and the surface emission transmitted through the atmosphere, which many studies have tried to accurately quantify (Kiehl & Trenberth, 1997; Trenberth et al., 2009; Trenberth & Fasullo, 2012; Stephens et al., 2012; Wild et al., 2013). For example, a widely cited diagram of Kiehl and Trenberth (1997) quantified the surface emission transmitted through the mid-infrared atmospheric window to be 40 W m^{-2} , which was revised by Costa and Shine (2012) to be 22 W m^{-2} using an accurate radiative transfer model. However, this latter number is still subject to the uncertainties due to the use of annually averaged atmospheric profiles in the calculation.

In comparison to the surface contribution, the layer-by-layer atmospheric contribution to OLR has been rarely quantified, despite the foreseeable benefits. Quantifying the contribution of different vertical layers to OLR would help visualize the radiative transfer process in the atmosphere and understand how importantly different parts of the atmosphere influence the TOA radiation balance. Moreover, from the remote sensing point of view, the identification of critical layers where most OLR photons originate from would illuminate which part of the atmosphere the space measurement of OLR is sensitive to. This would elucidate the theoretical basis of passive satellite sounding of the atmosphere. Hence, in this paper, we are motivated to use the latest global reanalysis atmospheric data and accurate radiative transfer calculations to provide an assessment of the vertically decomposed atmospheric contributions, as well as surface contribution, to OLR.

As evidenced by many previous studies, spectrally decomposed OLR provides much richer information about the atmosphere. For example, OLR spectral measurements were found to afford a rigorous test of the simulations of global climate models (GCMs) and provide useful clues for identifying the causes of the model biases (Y. Huang et al., 2007a; Y. Huang & Ramaswamy, 2008; X. Huang et al., 2008; Feldman et al., 2014). The rich information in the OLR spectra also makes it possible to spectrally fingerprint the radiative forcings and feedbacks that drive and modulate the global climate change (Brindley & Bantges, 2016; Harries et al., 2008; Y. Huang et al., 2010a; Y. Huang et al., 2010b; Y. Huang & Ramaswamy, 2009; Y. Huang, 2013; Whitburn et al., 2021). Hence, in addition to the total OLR, we are motivated to analyze spectrally decomposed OLR and how it is contributed by different atmospheric layers. We are especially interested to analyze the OLR with longer wavelength, i.e., in the conventionally termed far-infrared (FIR) spectral region (Harries et al., 2008). The interest in the FIR is motivated by the fact that a large fraction of the OLR energy exists in this spectral region (Harries et al., 2008; X. Huang et al., 2008; Chen et al., 2014; Turner & Mlawer, 2010; Bellisario et al., 2019; Martinazzo et al., 2021) and that the OLR in FIR is especially sensitive to atmospheric water vapor and clouds and thus provides potentially improved means of retrieving their information (Sinha & Harries, 1995; Harries et al., 2008; Delamere et al., 2010; Cox et al., 2015; L. Palchetti et al., 2015; L. Palchetti et al., 2016; Magurno et al., 2020; Blanchet et al., 2011).

In recognition of the importance of FIR, several observational projects have recently gained momentum in their development and aimed to acquire unprecedented measurements in this spectral region. These projects include the Thin Ice Cloud in Far Infrared Experiment (TICFIRE, Blanchet et al., 2011) funded by the Canadian Space Agency, the Polar Radiant Energy in the

Far Infrared Experiment (PREFIRE) funded by U.S. NASA (L'Ecuyer et al., 2021), and the Far-Infrared Outgoing Radiation Understanding and Monitoring (FORUM) project funded by the European Space Agency (L Palchetti et al., 2020). Given that the worldwide observation data of FIR is not available yet, we are motivated to use simulations to acquire prior knowledge of climatological mean distribution of the OLR in FIR.

In summary, in this paper we aim to use a radiative transfer model to simulate the spectrally decomposed OLR and dissect the atmospheric and surface contributions to the global mean OLR as well as its geographic distributions. We are particularly interested to identify the critical atmospheric layers that contribute most to the OLR in different spectral regions. The rest of the paper is structured as: Section 2 describes the model and dataset used for analyses. Section 3 presents the results of layer-wise contributions to OLR and their geographical patterns. Section 4 summarizes the main conclusions of the paper.

2. Method

2.1 Numerical model and data

In this paper, we use the GCM version of the longwave rapid radiative transfer model (RRTMG) (Mlawer et al., 1997) to simulate OLR. RRTMG has been extensively validated against the benchmark line-by-line computations (Collins et al., 2006). It adopts the correlated-k method, conducting the radiative transfer computation at 140 g-points (monochromatic spectral nodes) to derive the OLR in 16 different spectral intervals ("bands") ranging from 10 cm⁻¹ to 3250 cm⁻¹. Three of the RRTMG bands are located in the far-infrared (see Table S1). Taking advantage of the RRTMG band configuration, we adopt a practical definition of the far-infrared as the wavenumbers ranging from 10 to 630 cm⁻¹ and designate the sum of the fluxes in the first three RRTMG bands as the OLR in the far-infrared and denote it as *FIR*. In comparison, the sum of the rest bands, which include the mid-infrared window regions, is referred to as *MIR* (mid-infrared).

To separate the emission contribution from each atmospheric layer to the OLR at the TOA, we use the model-generated radiative properties at each g-point, including optical depth, blackbody emission, etc., to calculate the layer-wise contribution to spectral OLR (i.e., the emission by a layer that reaches the TOA), following the discrete form of radiative transfer equation (Goody & Young 1989):

$$I(\tau = 0) = B(\tau^*) \cdot e^{-\tau^*} + \sum_{i=1}^n [B(\tau_i) \cdot e^{-\tau_i} \cdot \Delta\tau_i] \quad (1)$$

where I is the upwelling irradiance at the TOA in the units of W m⁻² and can represent either *total OLR*, *FIR* or *MIR*. τ is the optical depth, monotonically increasing from the TOA ($\tau = 0$) to the surface (τ^*). τ_i is the optical depth between TOA and the i^{th} atmospheric layer and $e^{-\tau_i}$ measures the transmittance between this layer and the TOA. $\Delta\tau_i$ is the optical depth difference between the upper and lower boundaries of the i^{th} layer and measures the emissivity of the layer. $B(\tau_i)$ and $B(\tau^*)$ are the source functions, i.e., the blackbody emission by the i^{th} atmospheric layer and the surface, respectively, in the units of W m⁻². n is the number of the layers ($n + 1$ levels) in the atmosphere. Based on Equation (1), the contribution of the surface emission or an

arbitrary atmospheric layer to the OLR is $B(\tau^*)e^{-\tau^*}$ or $B(\tau_i)e^{-\tau_i}\Delta\tau_i$, respectively, which we compute from the RRTMG-generated optical depths and source functions.

To accurately measure the OLR in reality, profiles required by RRTMG, such as temperature, water vapor, ozone concentration, cloud fraction, cloud water path, etc., are taken from the 6-hourly data of the fifth generation European Centre for Medium-Range Weather Forecasts atmospheric reanalysis (ERA5) (Hersbach et al., 2020), with a horizontal resolution of 2.5 degree by 2.5 degree and 37 vertical levels. Five more layers of the U.S. standard profile are patched above 1hPa to ensure the accuracy of the radiative flux. Other cloud properties, such as cloud liquid droplet and ice crystal radii are taken from the synoptic TOA and surface fluxes and clouds product of the Clouds and Earth's Radiant Energy System (CERES, Doelling et al., 2013) at the same sampling time, interpolated from a horizontal resolution of 1 degree to the resolution (2.5 degree) of the ERA5 data.

To account for the seasonal variations of the spectral OLR, we conduct a one-year simulation in year 2013, a neutral year with no significant El niño or La niña anomalies (see Figure S1), using the instantaneous profiles described above. Annual mean results are averaged from all instantaneous radiative fluxes, i.e., $\frac{1}{365 \times 4} \sum_{i=1}^{365 \times 4} I_i$, where the index i indicates different time steps, and used for all the analyses here. We will focus on the all-sky results in the following, although clear-sky fluxes are also computed by excluding cloud condensates in the RRTMG computation and are compared to the all-sky results in order to measure the cloud effects.

The total OLR diagnosed based on Equation (1) is compared to the RRTMG directly output values as shown in Figure S2, which confirms the validity of this decomposition. Figure S2 also shows a comparison of total OLR between our simulation and the data provided by ERA5, which are in good agreement and affirms the quality of the simulation data used in this analysis.

2.2 Diagnostic method

From Equation (1), the contribution of a certain layer is controlled by two factors: the source function (the Planck term B relevant to the atmospheric temperature) and the radiative properties (the emissivity and transmission terms relevant to τ). To isolate the spectroscopic effect relevant to τ from the temperature effect that affects B , here we define a *layer contribution function*:

$$f_i = B(\tau_i) \cdot e^{-\tau_i} \cdot \Delta\tau_i \quad (2)$$

to distinguish from the often-used concept of *weighting function* (Goody & Yung, 1989):

$$w_i = e^{-\tau_i} \cdot \Delta\tau_i \quad (3)$$

Furthermore, we analyze these functions in their normalized forms:

$$F_i = \frac{f_i}{OLR_{atm} \cdot \Delta p_i} \cdot 100hPa \quad (4)$$

$$W_i = \frac{w_i}{(\sum w_i) \cdot \Delta p_i} \cdot 100 \text{hPa} \quad (5)$$

Here f_i and w_i are the layer contribution functions and weighting functions of the i^{th} layer, respectively. Δp_i is the pressure thickness of the layer, in the units of hPa. OLR_{atm} is the total atmospheric contribution to OLR and $\sum w_i$ is the sum of the weighting functions of all the atmospheric layers (excluding the surface), as the focus here is to dissect the atmospheric contribution. F_i measures the overall relative contribution of each 100hPa-thick atmospheric layer; in comparison, W_i measures the relative contribution governed by absorber distribution, i.e., the contribution that an isothermal atmosphere would have. Note that both functions, F_i and W_i , are defined here with respect to unit layer thickness measured in hPa and thus the latter differs from the weighting function ($\frac{de^{-\tau_i}}{dz}$) that is often used in remote sensing analyses and defined with respect to unit thickness in km.

Although the contribution function F_i can be evaluated from the band fluxes readily available from RRTMG, it would be inappropriate to simply average the RRTMG-computed transmission functions to obtain a broadband weighting function W_i , because such a straightforward average would not account for the strong variation of the radiance intensity with frequency (a feature of Planck function). Alternatively, we adopt a diagnostic approach to infer a band-representative optical depth using the flux profiles generated from RRTMG. Assuming a n -layer ($n+1$ levels) atmosphere with an increasing index from TOA to the surface, the flux coming into and out of the boundaries of i^{th} layer can be expressed as:

$$F_i^{up} = e^{-\Delta\tilde{\tau}_i} \cdot F_{i+1}^{up} + (1 - e^{-\Delta\tilde{\tau}_i}) \cdot \tilde{B}_i \quad (6)$$

$$F_{i+1}^{down} = e^{-\Delta\tilde{\tau}_i} \cdot F_i^{down} + (1 - e^{-\Delta\tilde{\tau}_i}) \cdot \tilde{B}_i \quad (7)$$

Here F_i^{up} and F_i^{down} are the upward and downward fluxes, respectively, at the upper boundary of the i^{th} layer in the units of W m^{-2} . Similarly, F_{i+1}^{up} and F_{i+1}^{down} are the fluxes at the lower boundary of the i^{th} layer. $\Delta\tilde{\tau}_i$ and \tilde{B}_i are the diagnostic optical depth and source function of the i^{th} layer, which can be solved from the two equations given all the fluxes available from RRTMG. We denote these diagnostic variables with a tilde to distinguish them from those directly generated by RRTMG.

From Equations (6) and (7), $\Delta\tilde{\tau}_i$ can be derived as:

$$\Delta\tilde{\tau}_i = \log\left(\frac{F_i^{down} - F_{i+1}^{up}}{F_{i+1}^{down} - F_i^{up}}\right) \quad (8)$$

Equation (8) provides a simple method to derive the optical depth throughout the atmospheric column. For instance, the accumulated optical depth of all layers above the i^{th} level can be computed as: $\tilde{\tau}_i = \sum_1^i \Delta\tilde{\tau}_j$. For readers interested in this topic, we show the geographic distribution of the derived broadband optical depth in the Supplementary Figure S3 and, as an example, compare the transmission profile based on the optical depth derived for one band and that averaged from the RRTMG-computed transmission functions at the g-points in Figure S4. The comparison shows that the diagnostic results can well depict the RRTMG-computed results, which we remind are not necessarily a better measure for the analysis here because they do not

account for the spectral variance of the radiance. See the Supplementary Information for further discussion of the calculation of the weighting function in different vertical coordinates (Figure S5).

The above formulation can be easily adapted to the analysis of either broadband or spectral OLR. For example, to obtain the weighting function appropriate to *FIR*, we use the RRTMG-simulated far-infrared fluxes (sum of the first three bands) to derive a FIR-appropriate optical depth profile following Equation (8) and then derive the weighting function following Equations (3) and (5). All the following results associated with broadband optical depth, transmittance or weighting function are obtained based on this method if not otherwise stated.

3. Results

In this section, we first present the geographic distribution of the *OLR* and *FIR* to provide a comparison of their global patterns. Following the methods introduced in Section 2, we then decompose the TOA fluxes into contributions from the different atmospheric layers and the surface. Finally, the cloud radiative effect is measured as the difference between all-sky and clear-sky results, to identify the cloud influence on the atmospheric layer-wise contributions to OLR. Our aim is to dissect the OLR distribution from a combined spectral, vertical and geographic perspective. Although the presentation below is focused on *OLR* and *FIR*, interested readers can find complementary *MIR* results in the Supplementary Information.

3.1 Geographic distribution of total OLR and FIR

Figure 1 shows the geographic distributions of the annual zonal mean OLR. There is a prominent meridional gradient of total OLR from the equator to the poles, with the maximum values in the tropics being about two times that at the South pole. In contrast, *FIR* displays a much more uniform pattern, showing little variations with latitudes (Figure 1a), although in both cases (total OLR and *FIR*), regional minima exist where high convective clouds (e.g., in the Intertropical Convergence Zone, ITCZ) or high topography (e.g., Tibet and Antarctic plateaus) result in colder radiating temperatures (Figure 1c and d).

It is interesting to notice that the fraction of the FIR flux relative to the total OLR increases with the latitude (Figure 1b), amounting to over 50% in North Pole and nearly 60% in South Pole. This is due to the shift of the peak of Planck function to lower wavenumbers at lower temperatures according to the Wien's displacement law. This emphasizes the predominant importance of FIR in the cold regions. This is in accordance with the previous studies; for example, Harries et al. (2008) noted a 45% FIR contribution to OLR.

The breakdown of the TOA FIR into atmospheric and surface contributions in Figure 1b discloses that the atmospheric fractional contribution (about 45%) is almost constant across the latitudes and the higher FIR fraction at the polar regions is mainly due to enhanced contributions from the surface, which is typically less than 1% in the lower latitudes (Table 1) due to the strong water vapor absorption but can amount to nearly 20% at South Pole where the atmosphere is thin and dry (Figure 1b). This indicates the opening of the atmospheric window in the far-infrared in the high latitude and high altitude regions, which makes the FIR measurements there especially useful for sounding both the atmosphere and possibly the surface (e.g., Feldman et al., 2014). A similar decomposition in MIR can be found in the Supplementary Figure S6.

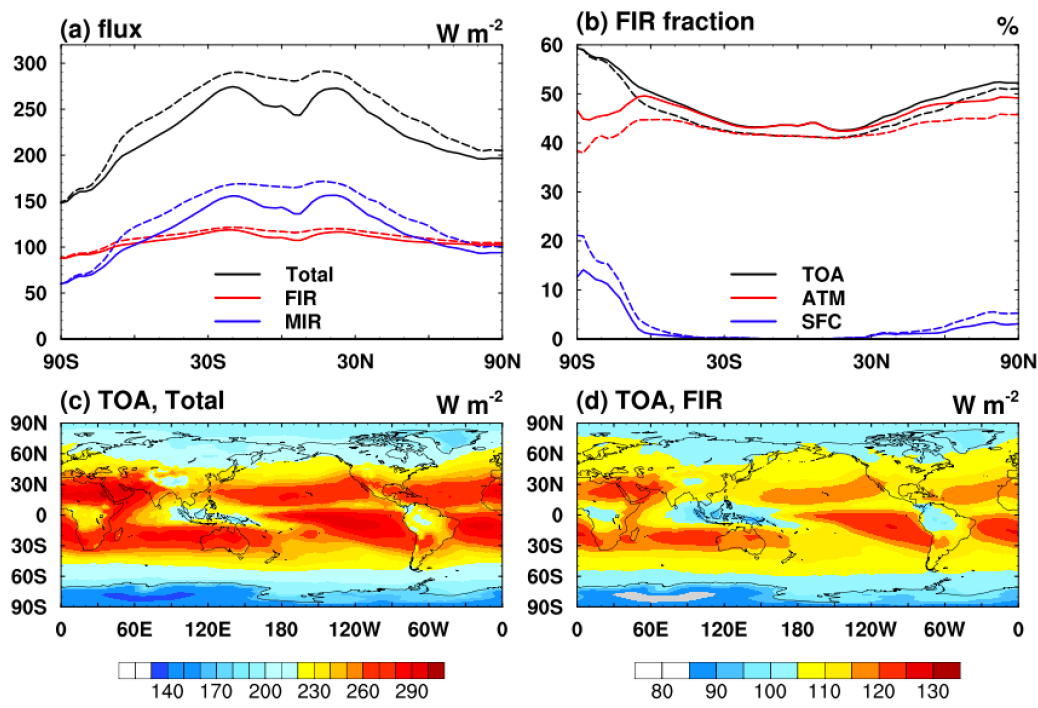


Figure 1. Annual mean distribution of OLR. (a) Zonal mean total OLR, FIR, units: W m^{-2} . (b) Zonal mean FIR fraction with respect to local total OLR, decomposed into contributions from the atmosphere and surface, units: %. (c, d) Geographic distributions of total OLR and FIR, units: W m^{-2} . Note that red and blue lines in (a, b) add up to the black lines. Solid lines in (a, b) represent the results in all sky and dash lines in clear sky.

(a)

W m ⁻² (%)		FIR	MIR	Total
TOA		110.51 (45.53%)	132.20 (54.47%)	242.72 (100.00%)
SFC		1.80 (0.74%)	39.56 (16.30%)	41.36 (17.04%)
ATM	whole	108.71 (44.79%)	92.64 (38.17%)	201.35 (82.96%)
	troposphere	99.61 (41.04%)	78.27 (32.25%)	177.88 (73.29%)
	stratosphere	9.11 (3.75%)	14.36 (5.92%)	23.47 (9.67%)

(b)

W m ⁻² (%)		FIR	MIR	Total
TOA		115.16 (43.48%)	149.68 (56.52%)	264.84 (100%)
SFC		2.86 (1.08%)	65.74 (24.82%)	68.59 (25.90%)
ATM	whole	112.30 (42.40%)	83.94 (31.70%)	196.25 (74.10%)
	troposphere	103.53 (39.09%)	69.73 (26.33%)	173.25 (65.42%)
	stratosphere	8.78 (3.31%)	14.22 (5.37%)	22.99 (8.68%)

(c)

W m ⁻²		FIR	MIR	Total
TOA		-4.65	-17.47	-22.12

SFC		-1.06	-26.17	-27.23
ATM	whole	-3.59	8.70	5.11
	troposphere	-3.92	8.55	4.63
	stratosphere	0.33	0.15	0.48

Table 1. Annual global mean contributions from the atmosphere and surface in the FIR and MIR to the total OLR in (a) all sky, (b) clear sky and (c) the cloud radiative effects (the difference of flux between all sky and clear sky). The contribution from troposphere and stratosphere is divided based on the definition of the tropopause of the World Meteorological Organization.

Table 1 summarizes the global mean contribution from each component to the total OLR in all sky. The global annual mean total OLR of 2013 is computed to be about 243 W m^{-2} , slightly higher than the value (239 W m^{-2}) reported in Trenberth et al. (2009) and that (240 W m^{-2}) in Loeb et al. (2018) but within the uncertainty range given by Stephens et al. (2012). From the global mean perspective, around 83% of the OLR is originated from the atmosphere and 45% (111 W m^{-2}) comes from FIR. The spatial variability (measured by the standard deviation of the local annual mean values across the globe as depicted in Figure 1c and d) of the total OLR is 30.86 W m^{-2} and that of FIR is 7.17 W m^{-2} , in accordance with the more uniform FIR pattern noted above. For the surface contribution, the global mean surface contribution is about 41 W m^{-2} , with the majority coming from the MIR. This number is close to the result of Kiehl and Trenberth (1997) and Trenberth et al. (2009), who reported that the transmitted surface emission is 40 W m^{-2} . In comparison, Costa and Shine (2012) measured the direct transmitted surface emission to be 22 W m^{-2} . The discrepancies between these numbers warrant some discussions. First, Kiehl and Trenberth (1997) particularly noted their number as transmission through the mid-infrared atmospheric window. If integrated from 820 to 1390 cm^{-1} (based on the RRTMG band partition), our calculation shows that the sum of OLR in this spectral range is 84.73 W m^{-2} , to which the surface contributes 33.29 W m^{-2} , showing significant atmospheric contribution even in these window bands as noted by Costa and Shine (2012). Secondly, the temporal and spatial resolution of profiles used in the computation can also lead to the differences. The result of Kiehl and Trenberth (1997) was presented for a single global mean profile and Costa and Shine (2012) used annual mean profiles, including that of clouds, in their radiative transfer calculation. In contrast, our simulation here uses 6-hourly instantaneous profiles at every location across the globe, minimizing the bias due to spatiotemporal sampling and nonlinear dependence of radiation on the atmospheric state variables. Although our simulation is also subject to certain limitations, for instance, the ignorance of cloud scattering of the infrared radiation, from the published assessments (e.g., Chen et al. 2014) this effect typically makes a difference of about 1 W m^{-2} in OLR and thus a small ($<1\%$) fractional uncertainty in our results.

To summarize, the results above disclose that the atmosphere makes a dominant contribution to OLR, especially in the far-infrared. The higher far-infrared fraction of OLR in the polar regions is caused by a stronger surface contribution as the atmospheric window opens in these dry regions. Given the importance of the atmospheric contribution, which critical layer of the atmosphere dominates the atmospheric contribution? Does the critical layer vary with the spectrum? We will address these questions in the following subsection.

3.2 Layer-wise contribution to total OLR and FIR

a) Global mean

First, we show a globally averaged spectral and vertical decomposition of OLR in Figure 2, which discloses that the critical layer that contributes most to OLR strongly varies in height in different spectral bands. In the far-infrared (wavenumber less than 630 cm^{-1}), the atmospheric contributions are mainly emitted from the middle and upper portions of the troposphere, with a maximum located at around 500hPa and 500 cm^{-1} (Figure 2a), due to the strong absorption of water vapor in this band blocking the emission from the lower troposphere and the surface. In the CO_2 absorption band (from 630 cm^{-1} to 700 cm^{-1}), the strong absorption of CO_2 masks almost all emissions below the stratosphere and leads to a contribution peak in the stratosphere. In the window region ($700\text{--}980\text{ cm}^{-1}$ and $1080\text{--}1180\text{ cm}^{-1}$), the atmosphere contribution is located in the lower troposphere where the relatively weaker water vapor continuum absorption mainly accounts for the atmospheric absorption and emission, and this allows the transmitted surface emission to make significant contribution to OLR (Figure 2c). The maximum in the stratosphere in the $980\text{--}1080\text{ cm}^{-1}$ band results from the absorption of stratospheric O_3 . It is interesting to note that Figure 2a, despite its much lower spectral resolution, well resembles the pattern of the sensitivity of spectral OLR to atmospheric perturbations (Huang et al., 2007b). This affirms that the critical layers that significantly contributing to OLR are also the vertical locations where the space OLR measurements are most sensitive to.

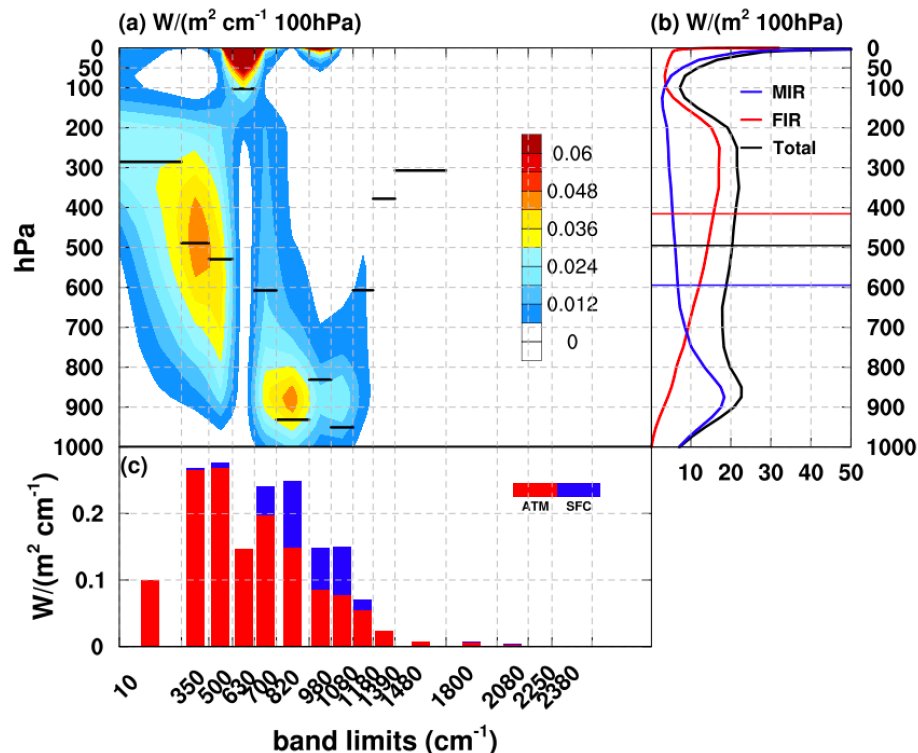


Figure 2. All-sky global annual mean spectral and vertical decomposition of OLR. (a) Layer-wise atmospheric contribution to the OLR irradiance flux in each of the 16 RRTMG bands, units: $\text{W}/(\text{m}^2\text{ cm}^{-1}\text{ 100hPa})$. (b) Spectrally integrated layer-wise contribution, units: $\text{W}/(\text{m}^2\text{ 100hPa})$. (c) Vertical integrated atmospheric contribution, in comparison with the surface

contribution, units: $W/(m^2 \text{ cm}^{-1})$. The horizontal lines in (a) and (b) are the inferred $\tau=1$ level using the diagnostic method described in Section 2. Note that the results in (a) and (b) are smoothed in the vertical direction using a 3-point running average to eliminate the artifacts caused by the non-uniform vertical resolution of the EAR5 atmospheric profiles; the same procedure is applied to the other vertical plots.

Despite the height variations of the critical layers from band to band, the broadband atmospheric contribution is rather vertically uniform throughout most of the troposphere (from 900hPa to 200hPa) (Figure 2b). This, however, is smoothed from the contrasting behaviors of FIR and MIR, to which the atmospheric contribution peaks in the upper and lower troposphere, respectively. The comparison to the clear-sky decomposition (Figure S7) shows that the local maxima near 900hPa and 200hPa are partially attributable to the significant cloud occurrence at these levels (see Figure S1e).

A remarkable finding revealed by Figure 2 is that the tropopause layer around 100hPa makes a minimum contribution to OLR. The atmospheric contribution here is about three times less than the surrounding vertical layers (Figure 2b). From Equation (1), is this due to the temperature minimum at the tropopause (the source function B_i) or the vertical distribution of the atmospheric absorbers and their spectroscopic features, which leads to a minimum of the weighting function value here? Figure 3 shows the comparison of F_i and W_i of total OLR and FIR, which shows that the contribution function is largely controlled by the shape of weighting function, with the temperature effect playing a modulating role. Specifically, in the troposphere below 600 hPa where the air temperature is relatively higher than the upper layers, the atmospheric contribution is nearly doubled by the temperature effect (in Figure 3a, the areas subtended by the two lines below 600hPa are 42.73% and 23.67%, respectively). The situation is opposite in the upper troposphere. However, at the tropopause around 100 hPa, the two lines coincide with each other, suggesting that the minimum contribution here is largely explained by the weighting function (atmospheric spectroscopy). The minimum contribution at the tropopause also indicates that it is generally more difficult to retrieve the atmospheric conditions near this level by using space measurements.

It is worth noting that the peaks of the weighting functions here (the black lines in Figure 3) differ from the often cited $\tau=1$ level (e.g., see the derivation of Huang & Bani Shahabadi 2014) as shown in Figure 2b. As Jeevanjee and Fueglistaler (2020) noted, the $\tau=1$ law depends on the choice of vertical coordinate and normally corresponds to the level where $\frac{de^{-\tau}}{dz}$ peaks, as opposed to where $\frac{de^{-\tau}}{dP}$ (the weighting function defined here) peaks.

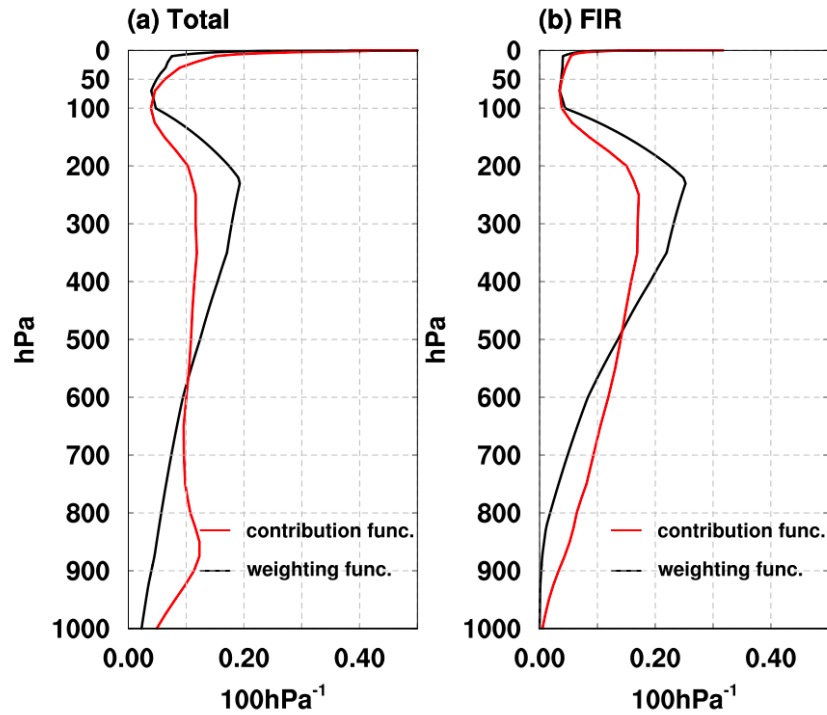


Figure 3. All-sky annual mean global mean contribution functions and weighting functions for (a) the total OLR, and (b) FIR.

b) Geographic variations

Figure 2 shows that the layer-wise atmospheric contributions with respect to the global mean OLR. How do the atmospheric contributions geographically vary? Figure 4 shows the zonal mean atmospheric contributions, in comparison with surface contribution. With regard to the total OLR, the atmospheric contribution shows a pattern that corresponds to the distribution of clouds. For instance, the maxima at 200hPa in the tropics, 400hPa in the mid-latitudes and 900hPa in the southern latitudes all coincide with the high cloud occurrence in these regions (Figure S1e). The comparison to the clear-sky result (Figure S8) further affirms that these maximum contribution layers are caused by the clouds (see further analysis in the following section).

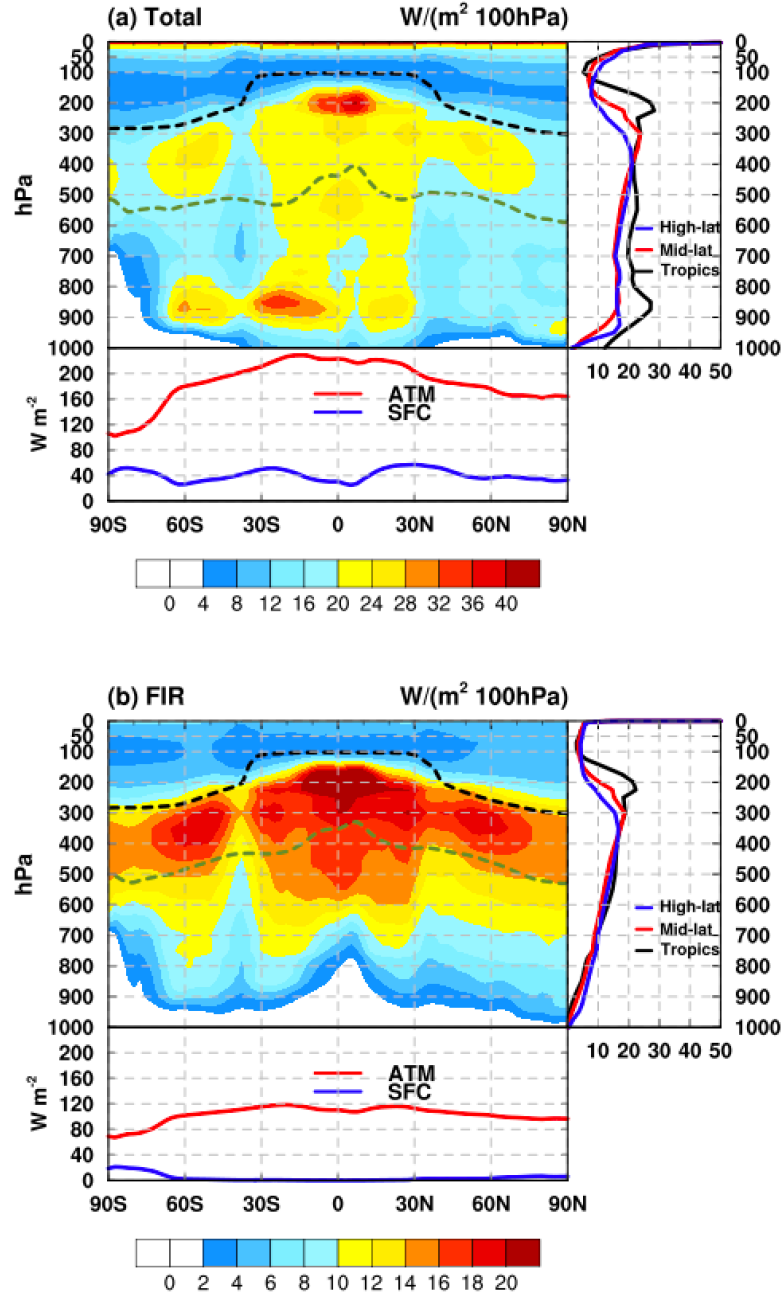


Figure 4. Annual mean and zonal mean flux intensity in all sky (a) in total OLR, (b) in FIR, units: $W/(m^2 \text{ 100hPa})$. The bottom line plots show the vertically integrated atmospheric contribution and surface contribution, units: $W \text{ m}^{-2}$. The right line plots are the regional averaged profiles, with Tropics representing the tropics (from 30N to 30S) and Mid-lat representing the northern mid-latitude region (60N-30N) and High-lat representing northern high-latitude region (90N-60N). The black dash line in contour plots represents the tropopause based on the definition of World Meteorological Organization and dark green dash line is the inferred $\tau = 1$ level using the method described in Section 2.

Comparing the overall atmospheric contribution to *OLR* to that of the surface, we find that interestingly the surface contribution is rather invariant with the latitude, showing a value of

about 40 W m^{-2} , although the atmospheric contribution peaks in the lower latitudes due to the higher emitting temperatures and greater atmospheric opacity there. The right line plot in Figure 4a contrasts the contribution functions between the northern-hemisphere low-, mid- and high-latitudes, which shows the local maximum in the upper troposphere descending from 200hPa in the low latitudes to in the 400hPa latitudes, reflecting the lowering of the tropopause which caps the atmospheric emitters such as clouds and water vapor within the troposphere. It is interesting to note that the aforementioned minimum contribution layer around the tropopause persists at all the latitudes, indicating that this feature is robust and prominent at all locations.

In comparison to the total OLR, the atmospheric contribution to *FIR* at all latitudes has a prominent maximum located right below the tropopause (around 200hPa to 400hPa). This is because the strong absorption in the water vapor rotational band in the far-infrared masks the emission from the lower troposphere and surface (blank regions in Figure 4b). This figure shows that only near the poles the near-surface atmospheric layers and the surface are visible to the space in the far-infrared.

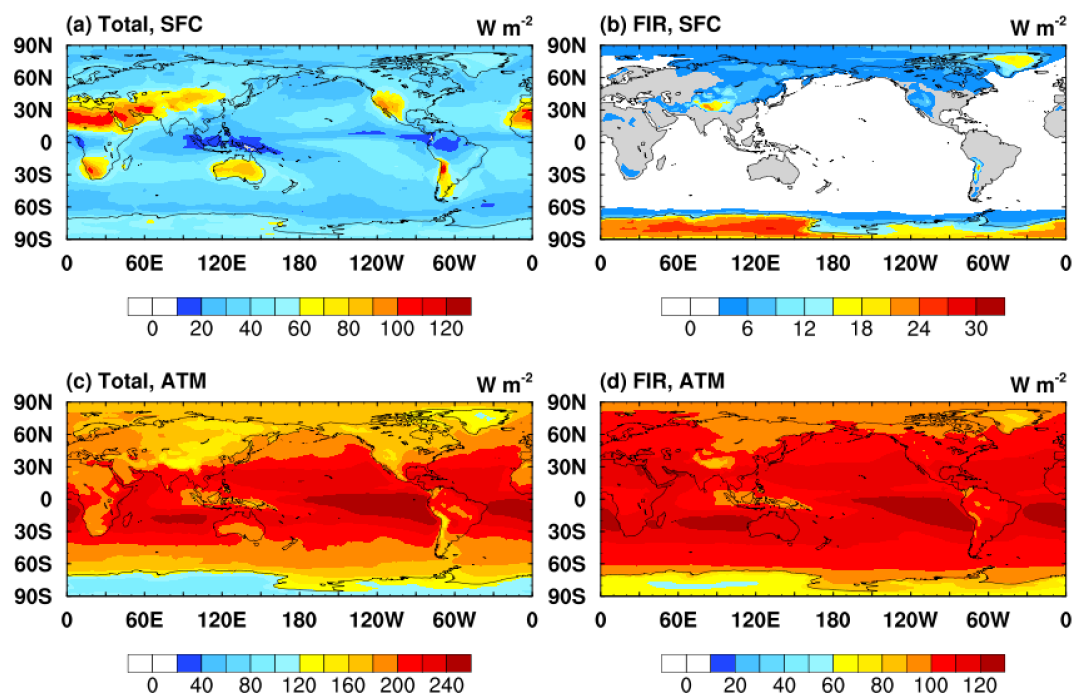


Figure 5. All-sky annual mean (a, b) surface and (c, d) atmospheric contributions to total OLR and FIR, units: W m^{-2} (See further decomposition of troposphere and stratosphere in Figure S9).

Figure 5 further discloses the geographic distribution of the surface and atmospheric contributions. The surface contribution to the total OLR is rather uniform across the globe at a value around 40 W m^{-2} , except in dry or high-elevation regions (e.g., Sahara, Tibet Plateau, Australia, Rocky Mountains and Andes) where the contribution can exceed 100 W m^{-2} , and in very moist regions such as the ITCZ where the surface contribution is lower than 20 W m^{-2} . Due to strong absorption in the water vapor rotational band, the surface contribution to FIR is visible only in polar regions and in regions of high topography (thin atmosphere).

447 Interestingly, the atmospheric contribution in the ITCZ also appears a local minimum
448 within the tropics, while the maxima locate in the subtropical regions where it is less cloudy and
449 thus more lower tropospheric emission at higher temperatures can reach the space.

450 In summary, this section investigates the layer-wise atmospheric contributions to total
451 OLR and FIR, as controlled by both temperature and spectroscopic effects, and compare the
452 atmospheric contribution to the surface contribution. We find that OLR, as well as its geographic
453 variation, is largely contributed by the atmosphere, although there are also noticeable regional
454 differences in the surface contribution, especially for the FIR. The vertical decomposition of the
455 atmospheric contribution clearly signifies the effects of clouds, which we will further analyze in
456 the following subsection.

459 3.3 Cloud radiative effect

460
461 Here, we use the difference in flux contribution between the all-sky and clear-sky to define
462 the cloud radiative effect (CRE). Figure 6a shows how clouds modify the global mean
463 atmospheric and surface contributions to the total OLR. Generally speaking, the atmospheric
464 contribution is enhanced at the locations of high cloud occurrence, e.g., at levels near 200hPa
465 and 900hPa (Figure S1e) as they enhance the atmospheric emissivity. At the same time, the
466 clouds decrease the transmission from layers below and reduce their contributions to OLR.

467 Figure 6b shows that interestingly the cloud effect in the far-infrared is to reduce the
468 overall atmospheric contribution (as indicated by a larger area of negative values subtended by
469 the red line) while the cloud effect in the mid-infrared is to increase the atmospheric
470 contribution, which, however, is at the price of reduced surface contribution. These effects lead
471 to a reduced OLR value in the all sky (243 W m^{-2} , as shown in Table 1) compared to clear sky
472 (265 W m^{-2}).

473 Figure 6c displays the spectral decomposition of the CRE and how it is decomposed into
474 atmospheric and surface contributions. As noted by many previous studies (e.g., Kiehl &
475 Trenberth 1997), the CRE mainly arises from the mid-infrared window. Overall, the cloud
476 effects increase the atmospheric contribution by 5.11 W m^{-2} and decrease that by the surface by -
477 27.23 W m^{-2} (Table 1b), leading to a total CRE at the TOA of 22.12 W m^{-2} . These numbers lie
478 within the range of values reported by others. For example, L'Ecuyer et al. (2008) measured the
479 total CRE to be 21.6 W m^{-2} using the CloudSat dataset, CERES Energy Balanced and Field Ed
480 4.1 Data Quality Summary reported 26 W m^{-2} in the CERES Ed 4.1 dataset, and Allan (2011)
481 reported 27.2 W m^{-2} , with atmosphere and surface contributions of 5.5 m^{-2} and -32.7 m^{-2}
482 respectively.

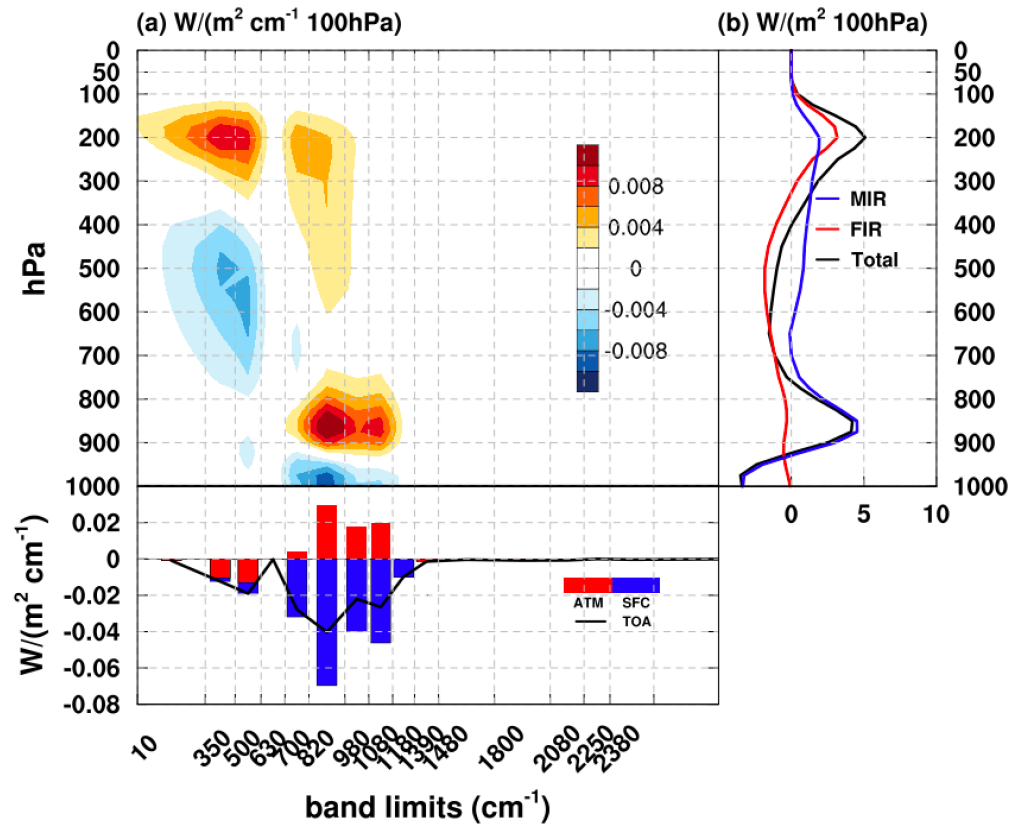


Figure 6. Similar to Figure 2 but for the cloud radiative effect.

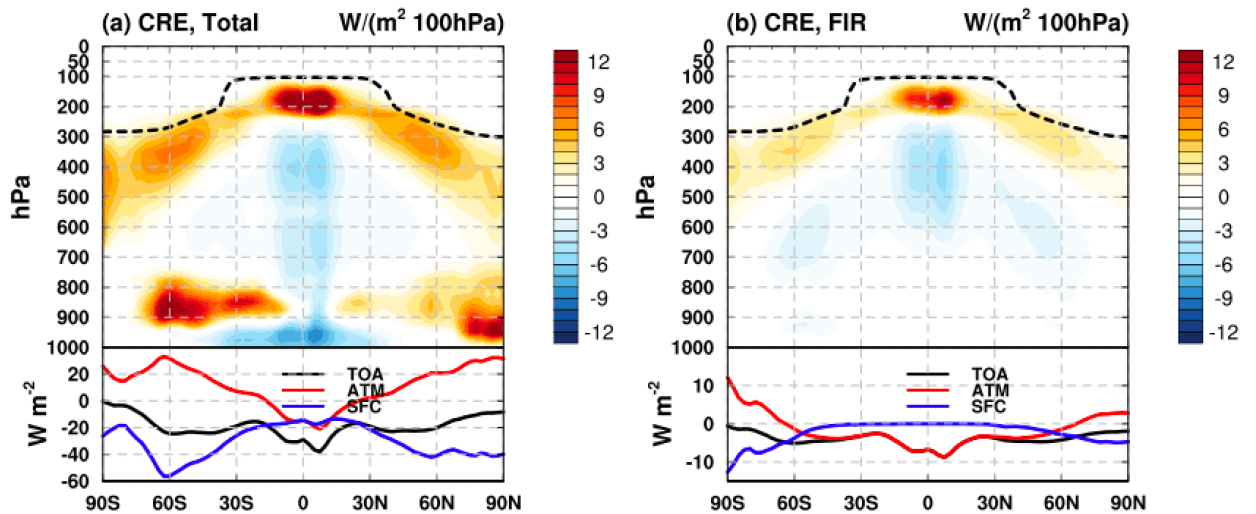


Figure 7. All-sky annual zonal mean cloud radiative effect on the atmospheric and surface contributions to (a) the total OLR, and (b) FIR, units: $W/(m^2 100hPa)$. Line plots show the vertically integrated atmospheric contribution and surface contribution, units: $W m^{-2}$. The black dash line in contour plots represents the tropopause (See results in MIR in Figure S10).

Figure 7 discloses the zonal mean pattern of the CRE, with respect to vertically decomposed atmospheric contribution in terms of both total OLR and FIR. It is interesting to notice that the cloud blocking of the surface contribution more strongly exists in the extratropics, while for the atmospheric contribution, the CRE changes sign from low- to high-latitudes.

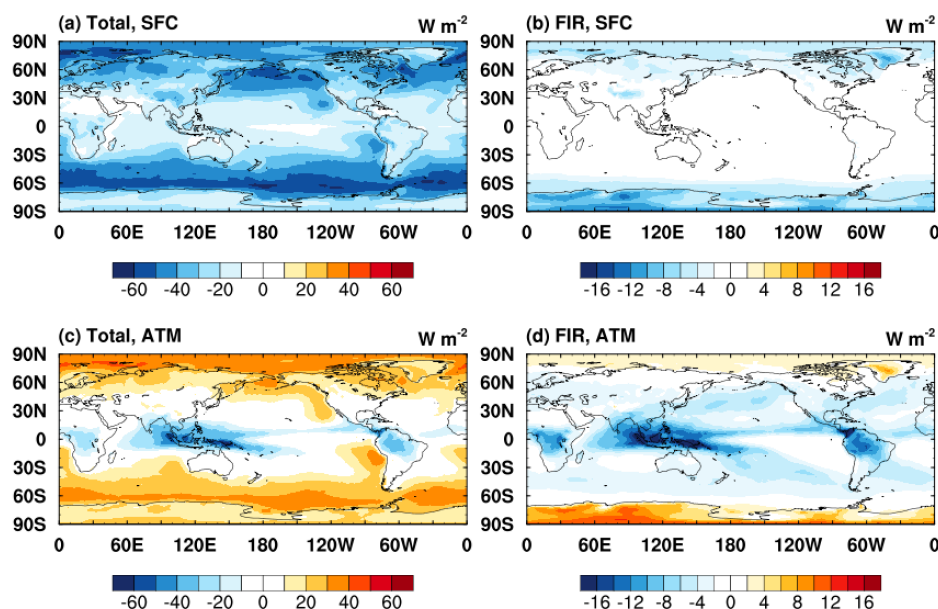


Figure 8. Annual mean cloud radiative effect on the surface and atmospheric contributions to (a, c) the total OLR and (b, d) FIR, units: W m^{-2} .

Figure 8 further shows the geographic distributions of the CRE. Clouds greatly decrease the transmission of the surface emission through the atmosphere and this effect is more significant in mid-to-high latitudes where the water vapor concentration is relatively lower compared with the tropics. With respect to the atmospheric contribution, the CRE is characterised by strong negative values at the ITCZ and positive values in the extratropics. The CRE in the atmosphere at different levels can be of opposite sign due to the compensation of enhanced emission at cloud layers and weakened transmission from cloud layers below (See more details in Figure S11 and Table S2).

In summary, clouds result in a decrease of the surface contribution to OLR and an increase of the atmospheric contribution to the TOA. The atmospheric contribution is especially enhanced at the locations of cloud occurrence.

4. Conclusions and discussions

In this paper, we use a radiative transfer model to simulate the spectrally resolved OLR and decompose it into the contributions from the surface and atmosphere. This analysis dissects OLR from a combined spectral, vertical and geographic perspective, identifying the critical atmospheric layers contributing most strongly to the OLR in different spectral bands and how the contributions vary geographically. A notable strength of this assessment is that it is based on a

whole year's instantaneous atmospheric profiles from an observationally constrained global dataset, ERA5.

One focus of this analysis is the global distribution of the OLR in the far-infrared, which is expected to be monitored by several new satellites under development. This study presents a preview of the observation based on simulated radiation fields. Our calculations affirm that a significant portion of the Earth thermal radiation to space, i.e., the total OLR, is radiated in the far-infrared. The far-infrared contribution is about 45% in terms of the global mean OLR and at colder polar regions this contribution can increase to about 60% (Table 1). The vertical decomposition discloses that the enhanced far-infrared contribution at the polar regions mainly results from the surface (as opposed to atmosphere) contribution (Figure 1b).

It has been a long-standing interest to quantify the surface contribution to OLR, for which previous studies reported differing values. We find that, from a global mean perspective, the surface contributes about 17% of OLR (Table 1). The distribution of zonally averaged surface contribution is relatively uniform across the globe with a strength of around 40 W m^{-2} , although the geographic distribution is modulated by the atmospheric thickness and moisture content (Figure 5). The surface contribution mainly comes from the mid-infrared, while in the far-infrared the surface is only visible in the polar regions where the far-infrared surface contribution can amount to 20% of the total OLR (compared to 1% or less at other latitudes).

Our analysis further resolves the atmospheric contributions to different vertical layers from TOA to surface and identifies the critical contribution layers in different spectral bands. We find the critical layers strongly vary in height in different spectral bands, with the critical layer in far-infrared being located in the upper troposphere while that in the mid-infrared in the lower troposphere (Figure 2). From a globally averaged and spectrally integrated point of view, the contribution to the broadband OLR is vertically uniform throughout most of the troposphere (Figure 2b). However, an interesting and remarkable feature revealed in this analysis is that the atmosphere around the tropopause makes minimum contribution to OLR and this is found to be a robust feature geographically at different latitudes (Figure 4a). By comparing the vertical contribution functions to the weighting functions obtained via a diagnostic technique developed here (Equation (4)), we find that the feature of minimum tropopause layer contribution is mainly due to the spectroscopic feature of the Earth atmosphere and to a smaller extent due to the temperature minimum around this level (Figure 3). Specifically, as shown in Figure 2a, the absorption strength of the major gas absorption bands is such that the Earth-escaping photons of OLR either emerges from the stratosphere (e.g., in the CO_2 band centered at 667 cm^{-1}) or from the troposphere (e.g., in the H_2O band in the far-infrared), making the tropopause layer a minimum contribution layer. It is for this reason that it is difficult to sound the tropopause layer by satellite observation of OLR from the space.

The cloud radiative effect on OLR primarily comes from the reduction of surface contribution (Table 1). In contrast, the cloud layers enhance the atmospheric contributions, especially at the location of the cloud layers. The cloud effect is much stronger in the mid-infrared than in the far-infrared, due to the existence of the mid-infrared atmospheric window ($800\text{-}1200 \text{ cm}^{-1}$) that is sensitive to the cloud masking effect (Figure 6).

In summary, our work provides a systematical assessment of the layer-wise contributions to OLR, pinpointing the critical atmospheric contributing layers in each spectral band and quantitatively comparing the atmospheric and surface contributions. Our simulation provides a modeling reference of spectrally decomposed global distribution of OLR and dissection of its spatial variability, which can be validated by future OLR observations that include the critical

far-infrared spectrum. This will provide insights into the radiation budget as well as model biases. While a climatologic mean distribution is presented here, the temporal variability of the OLR and how it results from varying atmospheric and surface contributions warrant further studies to elucidate.

Acknowledgements

We acknowledge grants from the Natural Sciences and Engineering Research Council of Canada (RGPIN-2019-04511) and the Fonds de Recherche Nature et Technologies of Quebec (2021-PR-283823) that supported this research.

Data Availability Statement

The ERA5 datasets can be accessed through the ECMWF website (<https://cds.climate.copernicus.eu/#!/search?text=ERA5&type=dataset>). The RRTM code can be downloaded at http://rtweb.aer.com/rrtm_frame.html. The data used in this work can be accessed from <http://dx.doi.org/10.17632/2d95dztpxn.1>.

References

- Allan, R. P. (2011). Combining satellite data and models to estimate cloud radiative effect at the surface and in the atmosphere. *Meteorological Applications*, 18(3), 324-333.
- Bellisario, C., Brindley, H. E., Tett, S. F., Rizzi, R., Di Natale, G., Palchetti, L., & Bianchini, G. (2019). Can downwelling far-infrared radiances over Antarctica be estimated from mid-infrared information? *Atmospheric Chemistry and Physics*, 19(11), 7927-7937.
- Blanchet, J.-P., Royer, A., Châteauneuf, F., Bouzid, Y., Blanchard, Y., Hamel, J.-F., . . . Pancrati, O. (2011). *TICFIRE: a far infrared payload to monitor the evolution of thin ice clouds*. Paper presented at the Sensors, Systems, and Next-Generation Satellites XV.
- Brindley, H., & Bantges, R. (2016). The spectral signature of recent climate change. *Current Climate Change Reports*, 2(3), 112-126.
- CERES ERAF Data Quality Summary, available online:
https://ceres.larc.nasa.gov/documents/DQ_summaries/CERES_EBAF_Ed4.1_DQS.pdf
- Chen, X., Huang, X., & Flanner, M. G. (2014). Sensitivity of modeled far - IR radiation budgets in polar continents to treatments of snow surface and ice cloud radiative properties. *Geophysical Research Letters*, 41(18), 6530-6537.
- Collins, W., Ramaswamy, V., Schwarzkopf, M. D., Sun, Y., Portmann, R. W., Fu, Q., . . . Forster, P. (2006). Radiative forcing by well - mixed greenhouse gases: Estimates from climate models in the Intergovernmental Panel on Climate Change (IPCC) Fourth Assessment Report (AR4). *Journal of Geophysical Research: Atmospheres*, 111(D14).
- Costa, S., & Shine, K. (2012). Outgoing longwave radiation due to directly transmitted surface emission. *Journal of the atmospheric sciences*, 69(6), 1865-1870.
- Cox, C. J., Walden, V. P., Rowe, P. M., & Shupe, M. D. (2015). Humidity trends imply increased sensitivity to clouds in a warming Arctic. *Nature communications*, 6(1), 1-8.
- Delamere, J., Clough, S., Payne, V., Mlawer, E., Turner, D., & Gamache, R. (2010). A far - infrared radiative closure study in the Arctic: Application to water vapor. *Journal of Geophysical Research: Atmospheres*, 115(D17).
- Doelling, D. R., Loeb, N. G., Keyes, D. F., Nordeen, M. L., Morstad, D., Nguyen, C., . . . Sun, M. (2013). Geostationary enhanced temporal interpolation for CERES flux products. *Journal of Atmospheric and Oceanic Technology*, 30(6), 1072-1090.
- Feldman, D. R., Collins, W. D., Pincus, R., Huang, X., & Chen, X. (2014). Far-infrared surface emissivity and climate. *Proceedings of the National Academy of Sciences*, 111(46), 16297-16302.
- Goody, R., & Young, Y. Atmospheric Radiation: theoretical basis, California Institute of technology. copyright Oxford University Press,(1961-1989).
- Harries, J., Carli, B., Rizzi, R., Serio, C., Mlynckzak, M., Palchetti, L., . . . Masiello, G. (2008). The far - infrared Earth. *Reviews of Geophysics*, 46(4).
- Hersbach, H., Bell, B., Berrisford, P., Hirahara, S., Horányi, A., Muñoz - Sabater, J., . . . Schepers, D. (2020). The ERA5 global reanalysis. *Quarterly Journal of the Royal Meteorological Society*, 146(730), 1999-2049.
- Huang, X., Yang, W., Loeb, N. G., & Ramaswamy, V. (2008). Spectrally resolved fluxes derived from collocated AIRS and CERES measurements and their application in model evaluation: Clear sky over the tropical oceans. *Journal of Geophysical Research: Atmospheres*, 113(D9).
- Huang, Y. (2013). A simulated climatology of spectrally decomposed atmospheric infrared

- radiation. *Journal of climate*, 26(5), 1702-1715.
- Huang, Y., & Bani Shahabadi, M. (2014). Why logarithmic? A note on the dependence of radiative forcing on gas concentration. *Journal of Geophysical Research: Atmospheres*, 119(24), 13,683-613,689.
- Huang, Y., Leroy, S., Gero, P. J., Dykema, J., & Anderson, J. (2010a). Separation of longwave climate feedbacks from spectral observations. *Journal of Geophysical Research: Atmospheres*, 115(D7).
- Huang, Y., Leroy, S. S., & Anderson, J. G. (2010b). Determining longwave forcing and feedback using infrared spectra and GNSS radio occultation. *Journal of climate*, 23(22), 6027-6035.
- Huang, Y., & Ramaswamy, V. (2008). Observed and simulated seasonal co - variations of outgoing longwave radiation spectrum and surface temperature. *Geophysical Research Letters*, 35(17).
- Huang, Y., & Ramaswamy, V. (2009). Evolution and trend of the outgoing longwave radiation spectrum. *Journal of climate*, 22(17), 4637-4651.
- Huang, Y., Ramaswamy, V., Huang, X., Fu, Q., & Bardeen, C. (2007a). A strict test in climate modeling with spectrally resolved radiances: GCM simulation versus AIRS observations. *Geophysical Research Letters*, 34(24).
- Huang, Y., Ramaswamy, V., & Soden, B. (2007b). An investigation of the sensitivity of the clear - sky outgoing longwave radiation to atmospheric temperature and water vapor. *Journal of Geophysical Research: Atmospheres*, 112(D5).
- Jeevanjee, N., & Fueglistaler, S. (2020). On the cooling-to-space approximation. *Journal of the atmospheric sciences*, 77(2), 465-478.
- Kiehl, J. T., & Trenberth, K. E. (1997). Earth's annual global mean energy budget. *Bulletin of the American meteorological society*, 78(2), 197-208.
- L'Ecuyer, T. S., Wood, N. B., Haladay, T., Stephens, G. L., & Stackhouse Jr, P. W. (2008). Impact of clouds on atmospheric heating based on the R04 CloudSat fluxes and heating rates data set. *Journal of Geophysical Research: Atmospheres*, 113(D8).
- L'Ecuyer, T. S., Drouin, B. J., Anheuser, J., Grames, M., Henderson, D. S., Huang, X., . . . Mateling, M. (2021). The Polar Radiant Energy in the Far Infrared Experiment: A New Perspective on Polar Longwave Energy Exchanges. *Bulletin of the American meteorological society*, 102(7), E1431-E1449.
- Magurno, D., Cossich, W., Maestri, T., Bantges, R., Brindley, H., Fox, S., . . . Warwick, L. (2020). Cirrus cloud identification from airborne far-infrared and mid-infrared spectra. *Remote Sensing*, 12(13), 2097.
- Martinazzo, M., Magurno, D., Cossich, W., Serio, C., Masiello, G., & Maestri, T. (2021). Assessment of the accuracy of scaling methods for radiance simulations at far and mid infrared wavelengths. *Journal of Quantitative Spectroscopy and Radiative Transfer*, 271, 107739.
- Mlawer, E. J., Taubman, S. J., Brown, P. D., Iacono, M. J., & Clough, S. A. (1997). Radiative transfer for inhomogeneous atmospheres: RRTM, a validated correlated - k model for the longwave. *Journal of Geophysical Research: Atmospheres*, 102(D14), 16663-16682.
- Palchetti, L., Bianchini, G., Di Natale, G., & Del Guasta, M. (2015). Far-infrared radiative properties of water vapor and clouds in Antarctica. *Bulletin of the American meteorological society*, 96(9), 1505-1518.
- Palchetti, L., Brindley, H., Bantges, R., Buehler, S., Camy-Peyret, C., Carli, B., . . . Dinelli, B. (2020). unique far-infrared satellite observations to better understand how Earth radiates

- energy to space. *Bulletin of the American meteorological society*, 101(12), E2030-E2046.
- Palchetti, L., Di Natale, G., & Bianchini, G. (2016). Remote sensing of cirrus cloud microphysical properties using spectral measurements over the full range of their thermal emission. *Journal of Geophysical Research: Atmospheres*, 121(18), 10,804-810,819.
- Sinha, A., & Harries, J. E. (1995). Water vapour and greenhouse trapping: The role of far infrared absorption. *Geophysical Research Letters*, 22(16), 2147-2150.
- Stephens, G. L., Li, J., Wild, M., Clayson, C. A., Loeb, N., Kato, S., . . . Andrews, T. (2012). An update on Earth's energy balance in light of the latest global observations. *Nature Geoscience*, 5(10), 691-696.
- Trenberth, K. E., & Fasullo, J. T. (2012). Tracking Earth's energy: From El Niño to global warming. *Surveys in geophysics*, 33(3), 413-426.
- Trenberth, K. E., Fasullo, J. T., & Kiehl, J. (2009). Earth's global energy budget. *Bulletin of the American meteorological society*, 90(3), 311-324.
- Turner, D., & Mlawer, E. (2010). The radiative heating in underexplored bands campaigns. *Bulletin of the American meteorological society*, 91(7), 911-924.
- Whitburn, S., Clarisse, L., Bouillon, M., Safieddine, S., George, M., Dewitte, S., . . . Clerbaux, C. (2021). Trends in spectrally resolved outgoing longwave radiation from 10 years of satellite measurements. *npj climate and atmospheric science*, 4(1), 1-8.
- Wild, M., Folini, D., Schär, C., Loeb, N., Dutton, E. G., & König-Langlo, G. (2013). The global energy balance from a surface perspective. *Climate dynamics*, 40(11), 3107-3134.